Ordering of a nanoconfined water network around zinc Ions induces high proton conductivity in layered titanate

Seongkoo Kang, Kyle G Reeves, Ivette Aguilar, Ana Gabriela Porras Gutierrez, Jean-Claude Badot, Serge Durand-Vidal, Christophe Legein, Monique Body, Antonella Iadecola, Olaf J Borkiewicz, et al.

Ordering of Nanoconfined Water Network around Zinc Ions Induces High Proton Conductivity in Layered Titanate

Seongkoo Kang,[a,b] Kyle G. Reeves,[a,b] Ivette Aguilar,[a,b] Ana Gabriela Porras Gutierrez, [a,b] Jean-Claude Badot,[b,c] Serge Durand-Vidal,[a,b] Christophe Legein,[d] Monique Body,[d] Antonella Iadecola,[b] Olaf J. Borkiewicz,[e] Olivier Dubrunfaut,[f] Franck Fayon,[g] Pierre Florian,[g] and Damien Dambournet*,[a,b]

[a] Sorbonne Université, CNRS, Physico-chimie des Electrolytes et Nanosystèmes Interfaciaux, PHENIX, F-75005 Paris, France

[b] Reseau sur le Stockage Electrochimique de l'Energie (RS2E), FR CNRS 3459, 80039 Amiens, France

[c] Chimie ParisTech, Université PSL, , Institut de Recherche de Chimie Paris, UMR CNRS 8247, 11 rue P. et M. Curie, 75005 Paris, France

[d] Institut de Molécules de Matériaux du Mans (IMMM) – UMR 6283 CNRS, Le Mans Université, Avenue Olivier Messiaen, 72805 Le Mans Cedex 9, France

[e] X-ray Science Division, Advanced Photon Source, Argonne National Laboratory, Lemont 60439, United States

[f] GeePs, Group of Electrical Engineering – Paris, UMR CNRS 8507, CentraleSupélec, Sorbonne Universités, Univ. Paris-Sud, Universite Paris-Saclay, 11 rue Joliot-Curie, 91192 Gif-sur-Yvette, France

[g] CNRS, CEMTHI UPR3079, Université d'Orléans, 45071 Orleans, France

ABSTRACT: We demonstrated that the chemical intercalation of Zn^{2+} ions within the interlayer space of the structure of a disordered layered titanate results in a drastic increase of the room temperature bulk proton conductivity from $8.11 \cdot 10^{-5}$ $S.m^{-1}$ for the *pristine* to $3.7 \cdot 10^{-2}$ $S.m^{-1}$ for *Zn-titanate.* Because of the crystallographic disordered nature of these compounds, we combined different techniques to establish the structural-transport relationships. Pair distribution function revealed that upon chemical insertion of Zn^{2+}, the local lepidocrocite arrangement is maintained, providing a suited model to investigate the effect of chemically intercalated ions on the transport properties and dynamics within the interlayer space. Broadband dielectric spectroscopy (50 to 10^{10} Hz) enabled to establish that Zn^{2+} inclusion promotes proton-hopping by self-dissociation of H_2O molecules yielding high proton mobility. Using Zn-K edge EXAFS and chemical analyses (EDX, TGA, ^{1}H NMR), Zn^{2+} ions were shown to be stabilized by $ZnCl_2(H_2O)$ complex within the interlayer space. Such complexes induce an increase of the H-bonding strength as evidenced by ^{1}H NMR, yielding a fast proton motion. Molecular dynamic simulations highlighted proton transfer between water molecules from structural interlayer and bonded to Zn^{2+} ions. The increasing interactions between these water molecules favors proton transfer at the origin of the fast bulk proton conductivity, which was assigned to a Grotthuss-type mechanism taking place at long-range order. This work provides a better understanding of how ion-water interactions mediated ionic transport and opens perspectives into the design of ionic conductors that can be used in energy storage applications.

INTRODUCTION

With respect to bulk, nanoconfined water displays unique properties that have been investigated to understand the effect of nanoconfinement on processes such as self-dissociation of H_2O,[1] proton mobility,[2,3] ion transport[4] or chemical reactions[5] to name a few. These processes are prominent in broad fields spanning biology, prebiotic chemistry, or energy storage.[3,5,6]

Hydrated metal oxides are typically built from the stacking of inorganic layers separated by a single (or multiple) slab(s) of water molecules. Such structural features can be used to understand better water dynamics in confined space and how ion-water interactions affect the transport/redox properties. For example, Remsing et *al.* [7] studied the interactions of water molecules and potassium ions confined between sheets of MnO_2. Their simulations show an interplay between the nature of the water-ion interactions and the electron transfer rate. Mitchell et *al.*[8] showed that confined structural water molecules enable to stabilize the structure of tungsten oxide hydrate upon fast proton intercalation. Last but not least, Boyd et *al.*[9] revealed that ion intercalation into the layered birnessite electrode material is mediated by structural water.

The above-mentioned examples highlight how the use of layered materials featuring "nanoconfined fluids" has recently become an emerging approach in the field of electrochemical chemical energy storage.[6,10] A better understanding of the microscopic structure and dynamics of interlayer water molecules and how ions (either electrochemically or chemically intercalated) affect properties would be useful to implement these types of materials. In this work, we investigated how chemically intercalated zinc ions affect the above-mentioned

properties in a layered titanate structure. Remarkably, the incorporation of Zn^{2+} ions results in a dramatic increase of the proton conductivity, which is multiplied by a factor of 450, assigned to proton-hopping owing to the modulation of the H-bonding network generated by water ordering around zinc cations.

RESULTS and DISCUSSION

Synthesis and proton conductivity. The synthesis method used therein relies on the sol-gel process, which has been extensively used to rationally design and tailor the properties of layered transition metal oxides.[11] In a typical synthesis, we used titanium isopropoxide dissolved in alcohol and water as the hydrolysis agent. To avoid the formation of anatase TiO_2, we fixed the hydrolysis ratio h = nH_2O/nTi to 3.33 and the temperature to 90 °C.[12] The X-ray amorphous precipitated compound, in which the substitution of oxide by hydroxide anions leads to the formation of titanium vacancies (□) and H_2O molecules are located in the interlayer space, presents the following general formula $Ti_{2-x}\square_xO_{4-4x}(OH)_{4x}.nH_2O$ (x ~ 0.5 and n ~ 0.55). Using high-energy X-ray total scattering, we previously showed that its local structure consists of a layered lepidocrocite-type structure (*Immm*) **(Figure 1a)**. The structure of this compound (referred hereafter as *pristine*) then consists of titanate layers made of edge-sharing TiO_6 octahedra arranged in a zigzag configuration with a single slab of crystal water molecules.

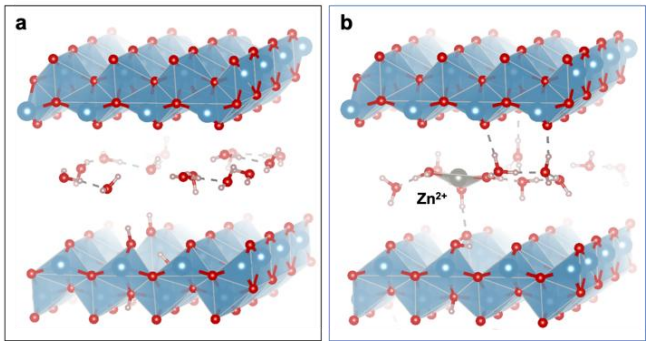

Figure 1. Structural representations of the *pristine* and *Zn-titanate*.

With a small ionic radius and a high charge, Zn^{2+} ion displays a high polarizing power, which can affect the structure of water molecules.[13,14] In our previous work investigating the electrochemical intercalation properties of such network, we showed the insertion reaction of Zn^{2+} in both the interlayer space (through the solvation of three water molecules, **Figure 1b**) and titanium vacancies were thermodynamically favorable.[15] However, using galvanostatic experiments revealed that the structure was not able to intercalate Zn^{2+} ions. Herein, we used a chemical route to stabilize Zn^{2+} ions in the titanate structure by adding zinc chloride ($ZnCl_2$) in the synthesis medium. The amount of Zn^{2+} stabilized in the structure can be controlled by tuning the content of zinc chloride precursor and several Zn/Ti molar ratios that are 0.1, 0.2, and 0.3 were used. X-ray energy-dispersive spectroscopy (EDX) revealed the presence of chloride anions with a constant amount of Zn:Cl of 1:2 **(Figure S2)**. In addition, EDX chemical mapping revealed that zinc and chloride are homogeneously distributed at the particle level ruling out the presence of impurity **(Figure S3)**. Finally, X-ray diffraction analysis **(Figure S4)** showed that upon zinc incorporation, the structure remains amorphous with diffuse scattering characteristic of a disordered material (referred hereafter as *Zn-titanate*).

Dielectric spectroscopy measurements were performed on the *pristine* and *Zn-titanate* to assess the effect of Zn^{2+} incorporation on transport properties. Note that thereafeter, we discussed the sample prepared for a Zn/Ti equals to 0.3. The inclusion of Zn^{2+} increases the RT bulk ionic conductivity by a factor of 450 from $8.11\cdot10^{-5}$ $S.m^{-1}$ for the *pristine* to $3.7\cdot10^{-2}$ $S.m^{-1}$ for *Zn-titanate* **(Figure 2)**. According to these values, Zn^{2+} inclusion induces a transition from an insulting to an ionic conductor.[16] Subsequently, the conductivities of the *pristine* and *Zn-titanate* samples obtained at temperatures ranging from 298 to 213 K follow an Arrhenius-based law as shown by their plot as a function of the inverse of the absolute temperature **(Figure 2)**. The linear relationships indicate that ionic mobility is a thermally activated process with activation energies of 0.51 eV for the *pristine* and 0.46 eV for *Zn-titanate*.

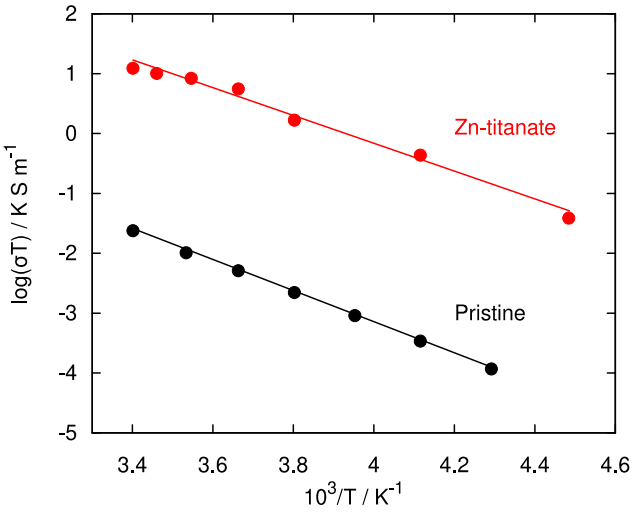

Figure 2. Arrhenius plot of the bulk conductivities for the *pristine* and *Zn-titanate*.

Structural features. Having established the drastic effect of chemically Zn^{2+} ions incorporation on the transport properties, we dug into the fundamentals behind this effect. Such rationalizing, however, faced challenges related to the crystallographic disordered nature of the structure, the unknown location and speciation of Zn^{2+} ions within the structure, and interlayer dynamics. To tackle these issues, we investigated the structural features by means of X-ray pair distribution function (PDF), Zn K-edge X-ray absorption spectroscopy, ^{1}H and ^{67}Zn solid-state NMR, broadband dielectric spectroscopy, and molecular dynamic simulation to dig further into the origin of the observed high ionic mobility.

High energy synchrotron X-ray total scattering measurements were performed on the *pristine* and *Zn-titanate*. PDF, which represents a histogram of interatomic distances, is particularly suited for studying disordered materials' atomic structure[17]. The PDFs of the *pristine* and *Zn-titanate* (**Figure 3**) feature similar peak positions confirming that both phases have similar local structures assigned to the lepidocrocite arrangement. In both cases, the peak intensities gradually

decrease for increasing inter-atomic distances and vanish when they are greater than 10 Å, which is a characteristic of X-ray amorphous compounds. The presence of Zn^{2+} produces minor changes to the PDF, yet noticeable. Notably, for the first peak corresponding to Ti–O(H) pair distance in TiO_6 octahedra (~1.98 Å), a shoulder, growing with the amount of $ZnCl_2$ added to the synthesis medium and then tentatively assigned to Zn–Cl bonds, is observed at 2.25 Å **(Figure S4)**. The intensity of the second peak located at 3.08 Å and corresponding to Ti···Ti distances between two edge-sharing octahedra, decreases indicating an increase of the titanium vacancies content. The third peak, which was primarily ascribed to Ti···O pairs in the titanate layers, shifts from 3.67 to 3.64 Å and its amplitude increases with the amount of $ZnCl_2$ added to the synthesis medium. An attempt to refine the PDF data **(Figure S4)** using a real-space approach indicated that this peak is not entirely captured by the lepidocrocite structure indicating that it is induced by the presence of Zn ions.

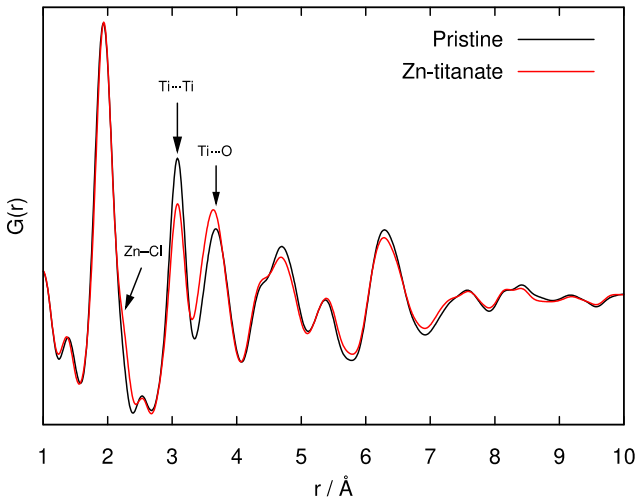

Figure 3. X-ray PDFs of *pristine* and *Zn-titanate*.

To better understand the local environment of Zn^{2+}, we conducted X-ray absorption spectroscopy at the Zn K-edge and ^{67}Zn high-field solid-state NMR. The latter, however, failed to provide a precise characterization of the environment of the Zn^{2+} ions. Despite an experimental time of ~36 h, the signal-to-noise ratio remains weak **(Figure S5)** which can be explained by the low zinc content in the sample combined with the properties of the ^{67}Zn nuclei, *i.e.*, low natural abundance, low gyromagnetic ratio and relatively large quadrupole moment Q.[18]

The Fourier transform of the X-ray absorption fine structure (EXAFS) oscillations of *Zn-titanate* is compared with those of ZnO and $ZnCl_2$ used as references (**Figure 4**). The first peak displays a broad feature with bond lengths ranging from those observed in $ZnCl_2$ (average bond length: 2.273 Å) to those observed in ZnO (1.978 Å), suggesting that in *Zn-titanate* the first coordination shell of zinc ions contains both oxide and chloride ions, in agreement with the occurrence of Zn-Cl bonds highlighted by the PDF data and EDX analysis. According to the value of the distance to the maximum of this asymmetric peak, Zn-Cl bonds are more numerous than Zn-O bonds.

To go further, we attempted to determine the chemical composition by assuming that $ZnCl_2$ is only located within the interlayer (see SI). The obtained phase composition is $Zn_{0.10}Cl_{0.20}Ti_{1.27}\square_{0.73}O_{1.11}(OH)_{2.89}\cdot 0.16H_2O$ pointing to a higher content of vacancies and lower hydration state compared to the pristine compound (about 0.5 H_2O are located within the interlayer space), which can be explained by the presence of $ZnCl_2$. Since EXAFS pointed to the presence of Zn-O bond, we postulated the presence of $ZnCl_2(H_2O)$ complex within the interlayer space, as further discussed below.

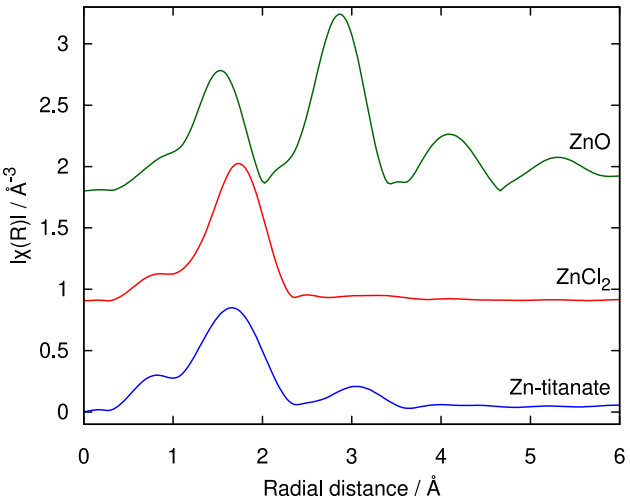

Figure 4. Fourier transform Zn K-edge EXAFS oscillations of *Zn-titanate* and for comparison ZnO and $ZnCl_2$.

To study the local chemical environment of proton, we used solid-state ^1H NMR. The ^1H MAS NMR spectra of the *pristine* and *Zn-titanate* (**Figure 5**) show similar features with three main resonances but the spectrum of *Zn-titanate* presents broader resonances due to larger isotropic chemical shift distributions and/or dipolar couplings, located at larger isotropic chemical shift (δ_{iso}) values. Both spectra were reconstructed **(Figures S8-S9, Table S1 & S2)** using several resonances that can be assigned to protons of structural H_2O molecules and OH groups coordinated by Ti atoms. According to the expected increase of ^1H δ_{iso} values with the coordination number of OH groups,[12,19] the peaks in the ranges 1–2 ppm and 4–5 ppm are assigned to Ti$\square$–OH/Ti$\square_3$–OH and Ti_2–OH/$Ti_2\square_2$–OH species, respectively.[12] At higher chemical shift, each spectrum presents a broad resonance which was deconvoluted with three and two lines, respectively. The three lines used for *pristine* have been assigned to OH groups from $Ti_3\square$–OH and Ti_4–OH species and protons of H_2O molecules. The proportion of each of these species cannot be determined in *Zn-titanate*. On the other hand, knowing the H_2O content in *Zn-titanate*, it is possible to estimate the proportions of one, two, three and fourfold coordinated OH groups (**Table 1**). Due to the higher rate of vacancies, the probabilities of existence of species threefold and fourfold coordinated with anions are lower in *Zn-titanate*. Moreover, OH groups are preferentially located in the vicinity of vacancies.[12] The proportion of $Ti_3\square$–OH and Ti_4–OH species is lower in *Zn-titanate* despite the higher proportion of OH groups among the anions. The shift to higher chemical shift values of the broad resonance assigned to OH groups from $Ti_3\square$–OH and Ti_4–OH species and to protons of H_2O molecules results from a lower H_2O content coupled with a higher average chemical shift of its protons, strongly sug-

gesting an increase of the strength of hydrogen bonds in the interlayer water network.[20,21]

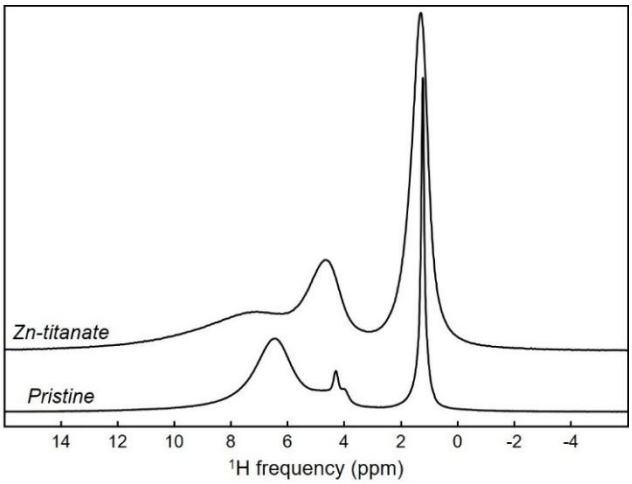

Figure 5. ^{1}H MAS NMR spectra of *pristine* (64 kHz) and *Zn-titanate* (60 kHz).

Table 1. Weighted average isotropic chemical shifts ($<\delta_{iso}>$), and the sum of relative intensities ($\sum$I) of the NMR resonances, according to their assignments, used for the fits of the ^{1}H MAS NMR spectra (see SI) of *pristine* and *Zn-titanate* (in italic) and relative intensities $I_{O\text{-}H}$ of protons from OH groups one, two and three and fourfold coordinated

Assignments	$<\delta_{iso}>$ (ppm)	$\sum$I (%)	$I_{O\text{-}H}$ (%)
Ti□–OH, Ti□$_3$–OH	1.27	30.4	45.5
	1.39	50.6	56.2
Ti_2–OH, Ti_2□$_2$–OH	4.67	16.1	24.1
	4.73	18.6	20.7
H_2O, Ti_3□–OH, Ti_4–OH	6.95	53.6	30.4
	7.59	30.8	23.1

Broadband dielectric spectroscopy. To better understand the origin of the increased bulk ionic conductivity, we used broadband (50–10^{10} Hz) dielectric spectroscopy to characterize the different frequency relaxation related to ionic motions and dipolar rotation of water molecules. We used complex permittivity $\varepsilon(\omega)$, which is more appropriate than the complex resistivity $\rho(\omega)$ or the conductivity $\sigma(\omega)$. The relations between the three properties can be described with equation 1 where ε_0 is the dielectric permittivity of vacuum ($\varepsilon_0 = 8.854 \cdot 10^{-12}$ F/m) and ω is the angular frequency.

$$\sigma(\omega) = \rho(\omega)^{-1} = i\omega\varepsilon_0\varepsilon(\omega) \qquad (1)$$

The complex dielectric permittivity originates from different frequency-dependent processes, such as microscopic fluctuations of molecular dipoles or the propagation of charge carriers.[22] The possible mechanisms in a layered material with confined water are the rotation of water, the charge hopping at high frequency, and the bulk polarizations at low frequency.[23]

Figure 6 shows the Nyquist plot of the imaginary part ε"(ω) *vs*. the real part ε'(ω) for the *pristine* **(Figure 6a)** and *Zn-titanate* **(Figure 6d)**. The diagrams are dominated by the slowest relaxation assigned to bulk conduction and polarization P1 (P'1), hiding the other relaxation processes. To distinguish the other processes, the Nyquist plot is decomposed with appropriate dielectric relaxation functions, which are presented below for a better understanding.

In an ideal condition where the interactions between dipoles are absent, the complex permittivity as a function of the field's frequency ω is described with the Debye function (equation 2), where ε_s and ε_∞ respectively correspond to the permittivity at the lowest and highest frequencies, and τ is the relaxation time.

$$\varepsilon^*(\omega) = \varepsilon_\infty + \frac{\varepsilon_s - \varepsilon_\infty}{1 + i\omega\tau} \qquad (2)$$

Non-Debye relaxations are, however, observed in most of the experimental data so the Debye function needs to be modified. The Cole-Cole (equation 3) function is a modified version of the Debye function where α is an empirical parameter related to the degree of departure from the Debye model.[24] The Debye and Cole-Cole functions are expressed by a semi-circle in the Nyquist plot.

$$\varepsilon^*(\omega) = \varepsilon_\infty + \frac{\varepsilon_s - \varepsilon_\infty}{1 + (i\omega\tau)^{1-\alpha}} \qquad (3)$$

The Havriliak–Negami equation (equation 4) is another empirical modification of the Debye relaxation model, enabling one to account for the asymmetry and broadness of the relaxation.[25] Havriliak-Negami function is commonly used to study molecular motions in disordered systems such as polymers or ion-conducting glasses.[26–29] The Havriliak-Negami function is characterized by a skewed arc.

$$\varepsilon^*(\omega) = \varepsilon_\infty + \frac{\varepsilon_s - \varepsilon_\infty}{(1 + (i\omega\tau)^{1-\alpha})^\beta} \qquad (4)$$

For *pristine* (and *Zn-titanate*), the decomposition of the Nyquist plot evidenced two other processes, named P2 (and P'2) and P3 (and P'3) that are respectively assigned to charge hopping and water rotation **(Table 2)**. The relaxation frequencies of P3 and P'3 were obtained using the Cole-Cole function. In both samples, the water rotation frequency is in the same order of magnitude with $2.7 \cdot 10^9$ Hz for the *pristine* and $5.4 \cdot 10^9$ Hz for *Zn-titanate*. For comparison purposes, we recall that the relaxation frequency of free water is $18 \cdot 10^9$ Hz.[30]

The second contribution related to charge hopping shows significant differences between the two samples. For the *pristine*, P2 was fitted using the Havriliak-Negami function at $4.3 \cdot 10^4$ Hz **(Figure 6b)**. Similar relaxation frequencies were measured in amorphous protonic conductors and assigned to proton hopping.[31] Hence, we attribute P2 to proton-hopping. In the absence of excess proton in the *pristine*, we assign the origin of such proton-hopping by the self-dissociation of H_2O molecules. The low ionic conductivity, however, showed that proton hopping proceeds only at the short-range order. High protonic conductivity is typically explained by a Grotthuss mechanism[32] involving long-range hopping. The occurrence of local proton hopping between neighboring water molecules indicates hydrogen bonds between two water molecules (O–H···O). The activation energy (0.49 eV) associated with the proton hopping indicates mild hydrogen interactions.[16]

In the presence of Zn^{2+} ions, the P'2 contribution was fitted using the Cole-Cole instead of the Havriliak-Negami function. Since the latter is typically used for disordered systems, this suggests that Zn^{2+} ions induce an ordering effect. The obtained frequency assigned to charge hopping, $1.3 \cdot 10^8$ Hz, is much higher than for the pristine ($4.3 \cdot 10^4$ Hz), indicating higher mobility. A lower activation energy of 0.29 eV (0.49 eV for pristine) was also found and further supports the higher bulk

ionic conductivity of *Zn-titanate* compared to the *pristine* compound. Similar to the pristine compound, we assigned the charge hopping to proton-hopping by self-dissociation of H_2O molecules.

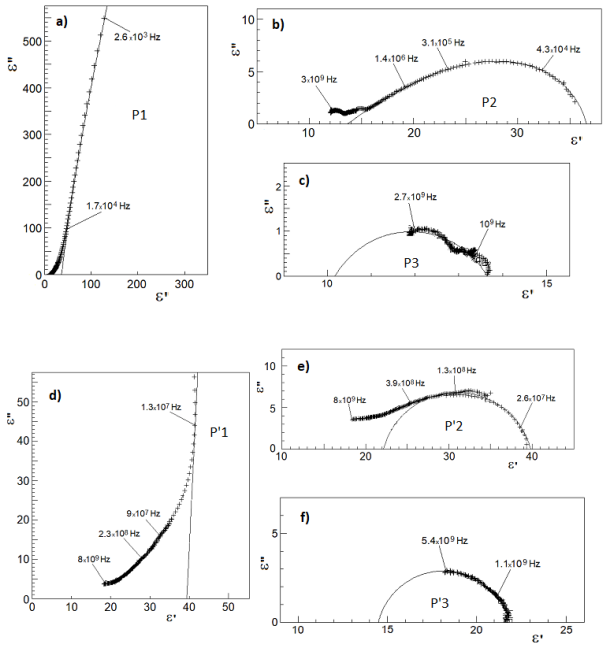

Figure 6. Nyquist plot of the imaginary part ε"(ω) vs. the real part ε'(ω) of the complex permittivity for *pristine* and *Zn-titanate* recorded at room temperature. a) Entire plot: only the contribution P1 is visible. b) Plot obtained upon the subtraction of P1: Evidence of the second relaxation P2. c) Plot obtained upon the subtraction of P2: Evidence of third relaxation P3. For *Zn-titanate*, the low-frequency part related to the total conductivity was subtracted previously. d) Entire plot: only the contribution P'1 is visible. e) Plot obtained upon the subtraction of P'1: Evidence of the second relaxation P'2. f) Plot obtained upon the subtraction of P'2: Evidence of third relaxation P'3.

To elaborate on the effect of Zn^{2+} insertion and its impact on the interlayer dynamics, for both samples an Arrhenius-based law was plotted for the proton and water relaxation frequencies **(Figure S10)**. Interestingly, for both samples the attempt frequency (ν_0) of the proton hopping yielded close values (Table 2). When plotting the activation energy of diffusion as a function of the proton relaxation frenquency obtained for both samples at 293 K, a linear relationship was established **(Figure 7)** confirming that the nature of the charge carrier, that is proton, is identical in both samples. In addition, the energy of proton migration is drastically reduced from 0.49 eV for the *pristine* to 0.29 eV for *Zn-titanate*. Furthermore, by considering that the activation energy of diffusion within the bulk (E_b) is the sum of the energy of proton migration and a term related to the energy of the number of mobile protons (E_n), the latter is equal to 0.02 eV for the *pristine* and 0.17 eV for *Zn-titanate*. The concentration *n* of mobile charge carriers (*i.e.*, H^+) that are thermally activated is given by: $n = N \exp\left(-\frac{E_n}{kT}\right)$, where N is the total number charge carriers. Using this law, the ratio of the number *n* of moving proton to the total number N of proton can be estimated, yielding 46 % for the *pristine* and 0.1 % for *Zn-titanate at 293 K*. This indicates that half of the water molecules in the *pristine* are in interactions, eventually yielding proton transfer (*i.e.*, water self-dissociation), which however only occurs at short-range order. The intercalation of Zn^{2+} induced a drastic decrease of the energy of migration of proton with diffusion that can occur at long-range order yielding a high ionic conductivity. The presence of zinc, however, seems also to trap protons as shown by the low concentration of mobile protons in *Zn-titanate*. This suggests that there might be an optimum in the Zn^{2+} concentration to reach the upper limit of proton conductivity in this material.

Table 2. Contributions, frequencies (at 293 K), activation energies, and bulk conductivities (at 293 K)of *pristine* and *Zn-titanate*.

Sample	Contribution	Charge hopping	Water rotation
Pristine	*Notations*	*P2*	*P3*
	Relaxation frequency (ν) (Hz)	$4.3 \cdot 10^4$	$2.7 \cdot 10^9$
	E_A (eV)	0.49	0.24
	Attempt frequency (ν_0) (Hz)	$9 \cdot 10^{12}$	$4 \cdot 10^{13}$
	Bulk conductivity, activation energy	$8.11 \cdot 10^{-5}$ S/m E_A = 0.51 eV	
Zn-titanate	*Notations*	*P'2*	*P'3*
	Relaxation frequency (ν) (Hz)	$1.3 \cdot 10^8$	$5.4 \cdot 10^9$
	E_A (eV)	0.29	0.25
	Attempt frequency (ν_0) (Hz)	$2 \cdot 10^{13}$	$9 \cdot 10^{13}$
	Bulk conductivity, activation energy	$3.7 \cdot 10^{-2}$ S/m E_A = 0.46 eV	

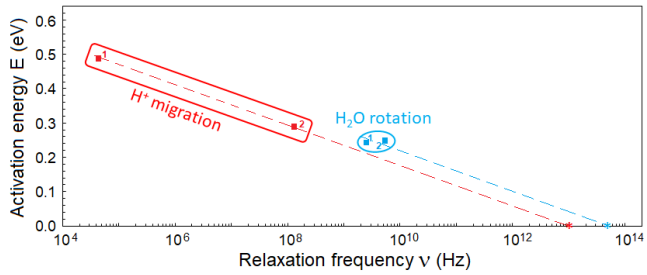

Figure 7. Activation energies Ea (eV) *vs*. relaxation frequencies ν (Hz) at 293 K attributed to proton migration (hopping) and water rotation in *pristine (1)* and *Zn-titanate (2)*: $E = 2.3kT \log \nu_0 - 2.3kT \log \nu$. The slope of dotted lines is *2.3kT* and gives the average frequency prefactors (attempt frequencies) ν_0 of about 10^{13} and 5×10^{13} Hz for proton migration (**red**) and water rotation (**blue**), respectively.

To summarize, as shown by PDF, the chemical insertion of Zn^{2+} ions can proceed without altering the layered lepidocrocite-type structure. EXAFS revealed that Zn-O and Zn-Cl bonds are stabilized in the compound, with Zn-Cl being predominant. ^{1}H NMR showed that the local environment reassembles that of the pristine compound with the presence of vacancies. Using BDS, the observed enhanced bulk ionic conductivity was assigned to proton hopping. According to EXAFS and the assessed chemical composition, we postulated

the presence of $ZnCl_2(H_2O)$ complex within the interlayer space. Such species were further used as a model to investigate the dynamic of water using first-principles molecular dynamics simulations.

First-principles molecular dynamics. To understand how Zn^{2+} ions affect the interlayer structure and dynamics (protons hopping), we used first-principles molecular dynamics performed on two simulation cells consisting of lepidocrocite structure without (*pristine*) and with Zn^{2+} ions (*Zn-titanate*). The pristine system was used as a reference to understand the effect of the Zn^{2+} ions within the interlayer space. For the *Zn-titanate*, the simulation cell contains one $ZnCl_2(H_2O)$ complex **(Figure 8a)**. This complex was shown to be stable throughout the 20 ps of the density functional theory molecular dynamics (DFTMD) simulation, further supporting the validity of the proposed model. The analysis thus shifts to investigate the impact that this transition metal complex has on the interlayer order and proton dynamics, both factors influencing the material's conductivity.

The dynamics of protons within the vicinity of the $ZnCl_2(H_2O)$ complex were investigated through the evolution of the two O-H bond lengths of the coordinated H_2O molecule as a function of the Zn-O distance at the corresponding time step of the simulation (**Figure 8b**). The results revealed that the Zn-O vibrational mode is dynamic with a large fluctuation of the distance. Such variation, however, does not seem to correlate with the O-H bond length. Most interestingly are the distinct behaviors of the two protons of the coordinated H_2O molecule, then differentiated as H1 and H2. In blue, H1 shows a greater likelihood of O-H bonds to break (d > 1.1Å), thus moving closer to its hydrogen-bonded neighbor. To visualize such an effect, we selected a configuration featuring a long O-H1 bond length of 1.25 Å. In the corresponding snapshot (**Figure 8c)**, the proton H1 is approximately equidistant to two oxygen atoms from the coordinated and free water molecules suggesting that these events enabled proton mobility, notably in the region of the Zn^{2+} ion.

To dig further into the impact of the Zn^{2+} ions, we looked at the arrangement of the interlayer water molecules. To do so, we considered the computed radial distribution function (RDF) between oxygen atoms only within the interlayer **(Figure 9)**. Such O···O distance represents a good descriptor of the proton dynamics since for distances of around 2.5 Å or below, the proton transfer barrier is low and eventually vanish because the electron shells of the donor and acceptor interpenetrate.[16,33]

The first peak corresponds to the O···O distance between two neighboring water molecules. The presence of Zn^{2+} ions induces a reduction of the average distance between oxygen atoms with a peak centered at 2.70 Å for the pristine and 2.65 Å for *Zn-titanate*. Additionally, the presence of Zn^{2+} ions induces a narrowing of the peak suggesting an ordering effect. Interestingly, the region between 3.1Å and 3.6Å shows a very low density of water molecules between first and second neighboring water molecules, suggesting a more rigid arrangement of water molecules at greater distances. This minimum, which approaches zero, is not observed in the pristine simulation (Figure 8, black), for example, nor in the RDF of bulk water as widely published in the literature[34]. We also consider the Cl-O RDF and the Cl-H RDF **(Figure S11)** to understand the local order around the chloride ions. We observed that water molecules generally approach the chloride ions to approximately 3Å with a preferred orientation placing one of the water's hydrogen atoms in between the chloride and the water's oxygen atom, but overall there is little structure in the RDF beyond this initial peak suggesting weakly hydrogen-bonded neighbors. This confirms that the ordering as presented in Figure 7 comes in great part from the coordinated water. Overall, these observations suggest an increase of the H-bond interactions induced by Zn^{2+} ions, in good agreement with solid-state ^1H NMR. The ordering effect induced by Zn^{2+} ions was also observed in the second solvation shell, with a more pronounced peak at ~4.5Å, suggesting a structuration of the interlayer water molecule network. These results show that the experimental measured high proton conductivity enabled by a Grotthuss-based mechanism is due to water ordering around the zinc complex.

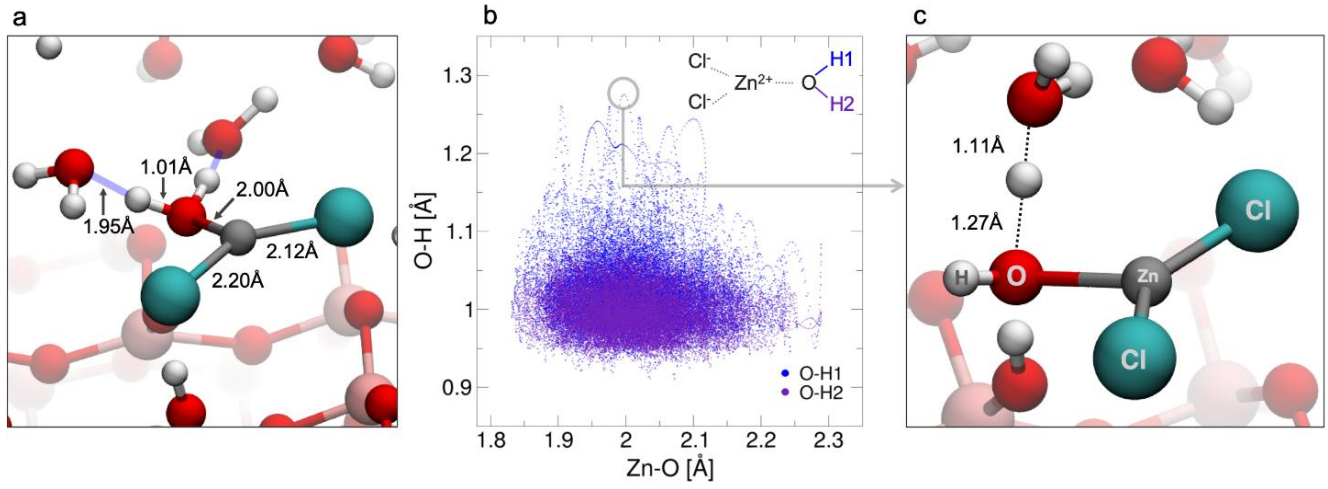

Figure 8. (*a*) Structural representation of $ZnCl_2(H_2O)$ complex used for the molecular dynamics simulations. (b) A scatter plot of bond lengths for Zn-O and the protons associated with the coordinated water molecule ($O\text{-}H_X$ where x = 1 (blue), 2 (purple)). Each point represents a timestep throughout the simulation. (c) snapshot at time A.

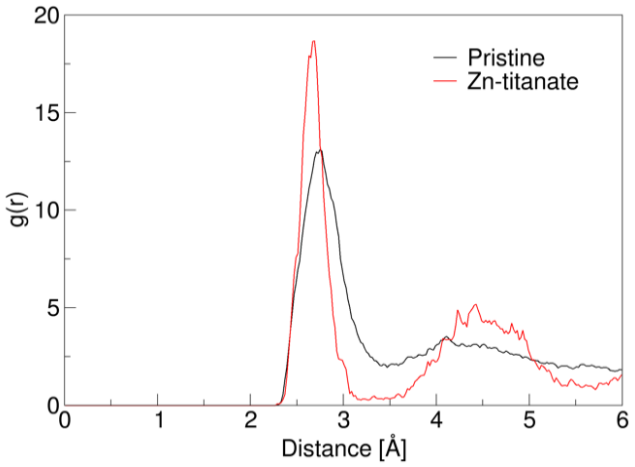

Figure 9. Radial distribution function of O-O within the interlayer space for the *pristine* and *Zn-titanate* obtained from DFTMD simulation.

CONCLUSION

We reported a chemical process relying on the sol-gel method to intercalate Zn^{2+} ions in a layered titanate structure. The analysis of the PDF data indicated that the local structure is that of the lepidocrocite with and without zinc inclusion. The measured bulk ionic conductivity highlighted a conductive change behavior moving from an insulating titanate to an ionic conductor for *Zn-titanate*. Broadband dielectric spectroscopy from 50 to 10^{10} Hz enabled to identify proton as the charge carrier responsible for the increase of bulk conductivity. In the absence of excess proton in the material, we attributed the ionic conductivity to proton transfer between interlayer water molecules. Molecular dynamic simulations showed that the zinc complex mediates the proton transfer through ordering of the hydrogen bonding network. This work opens a versatile chemical approach to tune the interlayer transport properties providing opportunities in the development of energy storage materials.

EXPERIMENTAL SECTION

Synthesis. Pristine: In a 45 mL Teflon-lined container, 4 mL of titanium (IV) isopropoxide (> 97 %, Sigma-Aldrich) was added into 25.19 mL of isopropanol (99.5 % min, Alfa Aesar) under stirring. Subsequently, we added 0.81 mL of ultrapure water (h = $[H_2O]/[Ti(OR)_4]$ = 3.33). The container was sealed in a stainless-steel autoclave and heated in an oven at 90 °C for 12 h to activate the precipitation thermally. The obtained white precipitate was recovered by centrifugation after being washed with ethanol (96 %), and it was dried in an oven overnight at 80 °C and then at 100 °C under vacuum.

Zn-titanate**:** two solutions were prepared with i) 4 mL of Ti (IV) isopropoxide (> 97 %, Sigma-Aldrich) dissolved in 10 mL of isopropanol (99.5 % min, Alfa Aesar) and ii) $ZnCl_2$ (Zn/Ti = 0.1, 0.2, and 0.3) dissolved in 15.19 mL of isopropanol and 0.81 mL of distilled water. The two solutions were then mixed in a Teflon-lined container. After 10 min of stirring, the container was sealed in a stainless-steel autoclave and heated in an oven at 90 °C for 12 h. The obtained gel was washed with ethanol, recovered by centrifugation, and dried overnight at 80 °C.

Broadband dielectric spectroscopy. The powder was pressed into pellets at 0.7 GPa (diameter = 3 mm, thickness = 1 mm) and metallized with silver paint. The pellets were placed between the inner conductor and a short-circuit of a coaxial APC7 cell.[35,36] The complex conductivity and permittivity data were collected between 50 and 10^{10} Hz with Agilent E4990A Impedance analyzer (50 to 10^8 Hz) and Keysight E8364b Network analyzer (10^7 to 10^{10} Hz). The measurement was performed between 298 and 213 K.

Energy dispersive X-ray Spectroscopy. The energy dispersive X-ray spectroscopy (EDX) analysis was performed with JEOL 2100-Plus transmission electron microscopy LaB_6 200 kV.

X-ray Diffraction. The powder X-ray diffraction was performed with Rigaku diffractometer equipped with Cu Kα radiation.

High energy X-ray total scattering. The high energy X-ray (λ = 0.2128 Å) scattering measurement was performed at the 11-ID-B beamline of Advanced Photon Source at Argonne National Laboratory. The 2D total scattering data were integrated into 1D diffraction data with FIT2D.[37] Subsequently, the data were Fourier transformed to PDFs after the correction using PDFgetX3.[38]

X-ray absorption spectroscopy. Synchrotron X-ray absorption spectroscopy was performed at the Zn K-edge at the ROCK beamline of the SOLEIL synchrotron facility (Saint-Aubin, France).[39] The Si(111) quick-XAS monochromator with an oscillation frequency of 2 Hz was employed to select the incident photons energy. The spectra were collected in transmission using three gas ionization chambers in series as detectors. A Zn metallic foil was placed between the second and the third ionization chambers to ensure the energy calibration. An average of 550 scans per spectrum (corresponding to 5 minutes of acquisition time for one merged XAS spectrum) was recorded to ensure the reproducibility and to increase the signal-to-noise ratio. The $ZnCl_2$ and ZnO reference samples were prepared by mixing the active material uniformly with carbon, then pressed into pellets of 10 mm in diameter.[40]

Thermogravimetric analysis. The thermogravimetric analysis was performed using TA instruments TGA 550 analyzer between 25 and 600 °C at a heating ramp of 1 °C/min under N_2 atmosphere. Zn-titanates were measured with Hi-Res™ TGA.[41]

Solid-state NMR. ^{1}H solid-state magic angle spinning (MAS) NMR experiments were performed on a Bruker Avance 300 spectrometer operating at 7.0 T (^{1}H Larmor frequency of 300.2 MHz), using a 1.3 mm CP-MAS probe head. The room temperature ^{1}H MAS spectra were recorded using a Hahn echo sequence with an interpulse delay equal to one rotor period. The 90° pulse length was set to 1.25 (2.4) µs and the recycle delays were set to 5 (20) s for *pristine* (*Zn-titanate*). ^{1}H spectra are referenced to TMS and were fitted using the DMFit software.[42]

In order to quantify the proton content on the *pristine* and *Zn-titanate* sample, ^{1}H solid-state MAS NMR (Hahn echo) spectra were also recorded for an organic crystalline solid, adamantane (Tricyclo[3.3.1.13,7]decane, $(CH)_4(CH_2)_6$) and the mass of each sample in the rotor were measured. The fits of the spectra allow one to determine the integrated intensities (I) for each sample. Since, for each sample, the recycle delays were chosen to ensure that the amount of signal detected is maximum (20 s for adamantane), we assume that the integrat-

ed intensities are proportional to the number of scans and the molar quantity of F atoms (n) in the rotor. The following values of ^{1}H wt.% have been deduced: 2.1 (±0.2) for *pristine* and 2.0 (±0.2) for *Zn-titanate*.

^{67}Zn NMR spectrum has been recorded on a Bruker Neo 850 spectrometer (20.0 T) operating at a frequency of 53.2 MHz. Sample has been packed in a 4 mm diameter zirconia rotor and, to overcome the probe's dead-time, a Hahn echo sequence under static conditions with a 40 µs inter-pulse delay has been used. Selective irradiation conditions have been assumed using a 24 kHz radio-frequency field and hence a T90 pulse of 3.5 µs. 256000 transients have been accumulated with a 0.5 s recycle delay (*i.e.*, a total acquisition time of approx. 36 h). ^{67}Zn chemical shifts were referenced to 1.0 M $Zn(NO_3)_2$ at 0 ppm.

Density Functional Theory Calculations. The DFT molecular dynamics simulations were performed using the CP2K via the Quickstep algorithm.[43,44] Kohn-Sham wavefunctions were constructed using DZVP-MOLOPT-SR-GTH basis sets and GTH pseudopotentials.[45] The electronic wavefunction cutoff was set to 400 Ry. The XC functional used in this work was PBE.[46,47] A geometry optimization was performed on a 4 × 4 × 1 lepidocrocite supercell made of two titanate layers, two interlayer water layers. The composition of the supercell is $Ti_{63}\square_1O_{124}(OH)_4{\cdot}32H_2O$, consistent with our previous work.[48] Ti^{4+} vacancies (□) remain charge neutral with four hydroxyl groups, the positions of which were determined in previous our work. We highlight the concentration of Ti^{4+} vacancies in the model system is lower than that of the experimental material, but the choice to include only one vacancy was made to simplify the analysis investigating the possible role of vacancies on the interlayer water dynamics.

Two NVT molecular dynamics simulations were launched. The first simulation was a pristine case in which the lepidocrocite structure described above has only water in the interlayer and was used as the control to compare local structure of the confined water. The second case is a simulation in which one $ZnCl_2$ was manually added to the simulation cell. Upon adding $ZnCl_2$ to the simulation cell, one water molecule was removed to account for the larger size of Cl^- ions. This is consistent with the experimental result that the lepidocrocite system with $ZnCl_2$ is observed to have a lower hydration state. The pristine and Zn-titanate simulations were each performed at 298 K with a time step of 0.5 fs for a total of 18ps and 17ps, respectively. Atoms in the titanate layers (except for the hydroxyl groups around the vacancy) were constrained to motion only within the plane and motion perpendicular to the titanate layer, which would result in a fluctuating interlayer distance, was forbidden. The interlayer was fixed at 11.5 Å.[49] Given the significant amount of motion of the surface hydroxyl groups observed in previous work, these atoms were not constrained in their motion.

Analyses of DFTMD trajectories. The initial 2ps of each simulation were discarded to account for the initial equilibration of the simulation. The RDF computed for the pristine case represents an average overall all oxygen atoms for all configurations throughout the 20ps trajectory, as each water molecule is considered to be equivalent. In the case of Zn-titanate, the RDF is computed setting 0 to be exclusively at the position of the oxygen atom bound to the zinc ion. In this way, possible induced order due to the Zn-complex could be more easily visualized. All RDF were computed in 2D to remove the contributions between water molecules in parallel planes of interlayer water.

ASSOCIATED CONTENT

Supporting Information.

Details of experimental characterizations including Electron dispersive X-ray spectroscopy; X-ray diffraction; X-ray Pair Distribution Function; ^{1}H, ^{67}Zn Magic Angle Spinning Nuclear Magnetic Resonance; Thermogravimetric analysis.

AUTHOR INFORMATION

Corresponding Author

* damien.dambournet@sorbonne-universite.fr

Notes

The authors declare no competing financial interest.

ACKNOWLEDGMENT

The work done at the Advanced Photon Source, an Office of Science User Facility operated for the U.S. Department of Energy (DOE) Office of Science by Argonne National Laboratory, was supported by the U.S. DOE under contract no. DE-AC02-06CH11357. We thank IMPC FR2482 for SEM-FEG instrumentation funded by CNRS, Sorbonne Université and C'Nano projets of Région Ile-de-France. XAS experiments were performed on the ROCK beamline (financed by ANR-10-EQPX-45) at SOLEIL Synchrotron, France. Financial support from the IR-RMN-THC Fr3050 CNRS for conducting the research is gratefully acknowledged.

REFERENCES

(1) Muñoz-Santiburcio, D.; Marx, D. Nanoconfinement in Slit Pores Enhances Water Self-Dissociation. *Phys. Rev. Lett.* **2017**, *119* (5), 056002.

(2) Muñoz-Santiburcio, D.; Wittekindt, C.; Marx, D. Nanoconfinement Effects on Hydrated Excess Protons in Layered Materials. *Nat. Commun.* **2013**, *4* (1), 2349.

(3) Tunuguntla, R. H.; Allen, F. I.; Kim, K.; Belliveau, A.; Noy, A. Ultrafast Proton Transport in Sub-1-Nm Diameter Carbon Nanotube Porins. *Nat. Nanotechnol.* **2016**, *11* (7), 639–644.

(4) Marcotte, A.; Mouterde, T.; Niguès, A.; Siria, A.; Bocquet, L. Mechanically Activated Ionic Transport across Single-Digit Carbon Nanotubes. *Nat. Mater.* **2020**, 1–5.

(5) Muñoz-Santiburcio, D.; Marx, D. Chemistry in Nanoconfined Water. *Chem. Sci.* **2017**, *8* (5), 3444–3452.

(6) Fleischmann, S.; Spencer, M. A.; Augustyn, V. Electrochemical Reactivity under Confinement Enabled by Molecularly Pillared 2D and Layered Materials. *Chem. Mater.* **2020**, *32* (8), 3325–3334.

(7) Remsing, R. C.; McKendry, I. G.; Strongin, D. R.; Klein, M. L.; Zdilla, M. J. Frustrated Solvation Structures Can Enhance Electron Transfer Rates. *J. Phys. Chem. Lett.* **2015**, *6* (23), 4804–4808.

(8) Mitchell, J. B.; Geise, N. R.; Paterson, A. R.; Osti, N. C.; Sun, Y.; Fleischmann, S.; Zhang, R.; Madsen, L. A.; Toney, M. F.; Jiang, D.; Kolesnikov, A. I.; Mamontov, E.; Augustyn, V. Confined Interlayer Water Promotes Structural Stability for High-Rate Electrochemical Proton Intercalation in Tungsten Oxide Hydrates. *ACS Energy Lett.* **2019**, *4* (12), 2805–2812.

(9) Boyd, S.; Ganeshan, K.; Tsai, W.-Y.; Wu, T.; Saeed, S.; Jiang, D.; Balke, N.; van Duin, A. C. T.; Augustyn, V. Effects of Interlayer Confinement and Hydration on Capacitive

Charge Storage in Birnessite. *Nat. Mater.* **2021**, *20* (12), 1689–1694.
(10) Augustyn, V.; Gogotsi, Y. 2D Materials with Nanoconfined Fluids for Electrochemical Energy Storage. *Joule* **2017**, *1* (3), 443–452.
(11) Uppuluri, R.; Sen Gupta, A.; Rosas, A. S.; Mallouk, T. E. Soft Chemistry of Ion-Exchangeable Layered Metal Oxides. *Chem. Soc. Rev.* **2018**, *47* (7), 2401–2430.
(12) Ma, J.; Reeves, K. G.; Porras Gutierrez, A.-G.; Body, M.; Legein, C.; Kakinuma, K.; Borkiewicz, O. J.; Chapman, K. W.; Groult, H.; Salanne, M.; Dambournet, D. Layered Lepidocrocite Type Structure Isolated by Revisiting the Sol–Gel Chemistry of Anatase TiO_2 : A New Anode Material for Batteries. *Chem. Mater.* **2017**, *29* (19), 8313–8324.
(13) Marcus, Y. Effect of Ions on the Structure of Water: Structure Making and Breaking. *Chem. Rev.* **2009**, *109* (3), 1346–1370.
(14) Zhang, Q.; Ma, Y.; Lu, Y.; Li, L.; Wan, F.; Zhang, K.; Chen, J. Modulating Electrolyte Structure for Ultralow Temperature Aqueous Zinc Batteries. *Nat. Commun.* **2020**, *11* (1), 4463.
(15) Kang, S.; Reeves, K. G.; Koketsu, T.; Ma, J.; Borkiewicz, O. J.; Strasser, P.; Ponrouch, A.; Dambournet, D. Multivalent Mg^{2+}-, Zn^{2+}-, and Ca^{2+}-Ion Intercalation Chemistry in a Disordered Layered Structure. *ACS Appl. Energy Mater.* **2020**, *3* (9), 9143–9150.
(16) Kreuer, K.-D. Proton Conductivity: Materials and Applications. *Chem. Mater.* **1996**, *8* (3), 610–641.
(17) Billinge, S. J. L.; Kanatzidis, M. G. Beyond Crystallography: The Study of Disorder, Nanocrystallinity and Crystallographically Challenged Materials with Pair Distribution Functions. *Chem. Commun.* **2004**, No. 7, 749–760.
(18) Harris, R. K.; Becker, E. D.; Menezes, S. M. C. de; Goodfellow, R.; Granger, P. NMR nomenclature. Nuclear spin properties and conventions for chemical shifts(IUPAC Recommendations 2001). *Pure Appl. Chem.* **2001**, *73* (11), 1795–1818.
(19) Crocker, M.; Herold, R. H. M.; Wilson, A. E.; Mackay, M.; Emeis, C. A.; Hoogendoorn, A. M. ^{1}H NMR Spectroscopy of Titania. Chemical Shift Assignments for Hydroxy Groups in Crystalline and Amorphous Forms of TiO_2. *J. Chem. Soc. Faraday Trans.* **1996**, *92* (15), 2791.
(20) Steiner, T. The Hydrogen Bond in the Solid State. *Angew Chem Int Ed* **2002**, 29.
(21) Wang, M.; Jaegers, N. R.; Lee, M.-S.; Wan, C.; Hu, J. Z.; Shi, H.; Mei, D.; Burton, S. D.; Camaioni, D. M.; Gutiérrez, O. Y.; Glezakou, V.-A.; Rousseau, R.; Wang, Y.; Lercher, J. A. Genesis and Stability of Hydronium Ions in Zeolite Channels. *J. Am. Chem. Soc.* **2019**, *141* (8), 3444–3455.
(22) Schönhals, A.; Kremer, F. Analysis of Dielectric Spectra. In *Broadband Dielectric Spectroscopy*; Kremer, F., Schönhals, A., Eds.; Springer Berlin Heidelberg: Berlin, Heidelberg, 2003; pp 59–98.
(23) Cadène, A.; Rotenberg, B.; Durand-Vidal, S.; Badot, J.-C.; Turq, P. Dielectric Spectroscopy as a Probe for Dynamic Properties of Compacted Smectites. *Phys. Chem. Earth* **2006**, *31*, 505–510.
(24) Cole, K. S.; Cole, R. H. Dispersion and Absorption in Dielectrics I. Alternating Current Characteristics. *J. Chem. Phys.* **1941**, *9* (4), 341–351.
(25) Havriliak, S.; Negami, S. A Complex Plane Representation of Dielectric and Mechanical Relaxation Processes in Some Polymers. *Polymer* **1967**, *8*, 161–210.
(26) Ikada, E.; Sugimura, T.; Watanabe, T. Dielectric Properties of Oligomers. VI. End-Group Effects in Vinyl Acetate and Methyl Methacrylate Oligomers. *J. Polym. Sci. Polym. Phys. Ed.* **1978**, *16* (5), 907–914.
(27) Ichikawa, K.; MacKnight, W. J. Dielectric Relaxation of Model Network Polymers. *Polymer* **1992**, *33* (22), 4693–4698.
(28) Ezquerra, T. A.; Majszczyk, J.; Baltà-Calleja, F. J.; López-Cabarcos, E.; Gardner, K. H.; Hsiao, B. S. Molecular Dynamics of the α Relaxation during Crystallization of a Glassy Polymer: A Real-Time Dielectric Spectroscopy Study. *Phys. Rev. B* **1994**, *50* (9), 6023–6031.
(29) Moynihan, C. T. Analysis of Electrical Relaxation in Ionically Conducting Glasses and Melts. *J. Non-Cryst. Solids* **1996**, *203*, 359–363.
(30) Buchner, R.; Barthel, J.; Stauber, J. The Dielectric Relaxation of Water between 0°C and 35°C. *Chem. Phys. Lett.* **1999**, *306* (1–2), 57–63.
(31) Hodge, I. M.; Angell, C. A. Electrical Relaxation in Amorphous Protonic Conductors. *J. Chem. Phys.* **1977**, *67* (4), 1647–1658.
(32) Agmon, N. The Grotthuss Mechanism. *Chem. Phys. Lett.* **1995**, *244* (5), 456–462.
(33) Borgis, D.; Tarjus, G.; Azzouz, H. An Adiabatic Dynamical Simulation Study of the Zundel Polarization of Strongly H- bonded Complexes in Solution. *J. Chem. Phys.* **1992**, *97* (2), 1390–1400.
(34) Wang, J.; Román-Pérez, G.; Soler, J. M.; Artacho, E.; Fernández-Serra, M.-V. Density, Structure, and Dynamics of Water: The Effect of van Der Waals Interactions. *J. Chem. Phys.* **2011**, *134* (2), 024516.
(35) Badot, J.-C.; Bianchi, V.; Baffier, N.; Belhadj-Tahar, N. Dielectric and Conductivity Spectroscopy of $Li_{1-x}Ni_{1+x}O_2$ in the Range of 10–1010 Hz: Polaron Hopping. *J. Phys. Condens. Matter* **2002**, *14*, 6917–6930.
(36) Badot, J. C.; Mantoux, A.; Baffier, N.; Dubrunfaut, O.; Lincot, D. Electrical Properties of V_2O_5 Thin Films Obtained by Atomic Layer Deposition (ALD). *J. Mater. Chem.* **2004**, *14* (23), 3411.
(37) Hammersley, A. P.; Svensson, S. O.; Hanfland, M.; Fitch, A. N.; Hausermann, D. Two-Dimensional Detector Software: From Real Detector to Idealised Image or Two-Theta Scan. *High Press. Res.* **1996**, *14* (4–6), 235–248.
(38) Juhás, P.; Davis, T.; Farrow, C. L.; Billinge, S. J. L. PDFgetX3 : A Rapid and Highly Automatable Program for Processing Powder Diffraction Data into Total Scattering Pair Distribution Functions. *J. Appl. Crystallogr.* **2013**, *46* (2), 560–566.
(39) Briois, V.; Fontaine, C. L.; Belin, S.; Barthe, L.; Moreno, T.; Pinty, V.; Carcy, A.; Girardot, R.; Fonda, E. ROCK: The New Quick-EXAFS Beamline at SOLEIL. *J. Phys. Conf. Ser.* **2016**, *712*, 012149.
(40) Ravel, B.; Newville, M. ATHENA, ARTEMIS, HEPHAESTUS: Data Analysis for X-Ray Absorption Spectroscopy Using IFEFFIT. *J. Synchrotron Radiat.* **2005**, *12* (4), 537–541.
(41) Gill, P. S.; Sauerbrunn, S. R.; Crowe, B. S. High Resolution Thermogravimetry. *J. Therm. Anal.* **1992**, *38* (3), 255–266.
(42) Massiot, D.; Fayon, F.; Capron, M.; King, I.; Le Calvé, S.; Alonso, B.; Durand, J.-O.; Bujoli, B.; Gan, Z.; Hoatson, G. Modelling One- and Two-Dimensional Solid-State NMR Spectra. *Magn. Reson. Chem.* **2002**, *40* (1), 70–76.
(43) Hutter, J.; Iannuzzi, M.; Schiffmann, F.; Vandevondele, J. CP2K: Atomistic Simulations of Condensed Matter Systems. *WIREs Comput. Mol. Sci.* **2014**, *4*, 15–25.
(44) VandeVondele, J.; Krack, M.; Mohamed, F.; Parrinello, M.; Chassaing, T.; Hutter, J. Quickstep: Fast and Accurate Density Functional Calculations Using a Mixed Gaussian and Plane Waves Approach. *Comput. Phys. Commun.* **2005**, *167* (2), 103–128.
(45) Goedecker, S.; Teter, M.; Hutter, J. Separable Dual-Space Gaussian Pseudopotentials. *Phys. Rev. B* **1996**, *54* (3), 1703–1710.
(46) Becke, A. D. Density-Functional Exchange-Energy Approximation with Correct Asymptotic Behavior. *Phys. Rev. A* **1988**, *38* (6), 3098–3100.

(47) Lee, C.; Yang, W.; Parr, R. G. Development of the Colle-Salvetti Correlation-Energy Formula into a Functional of the Electron Density. *Phys. Rev. B* **1988**, *37* (2), 785–789.
(48) Reeves, K. G.; Ma, J.; Fukunishi, M.; Salanne, M.; Komaba, S.; Dambournet, D. Insights into Li^+, Na^+, and K^+ Intercalation in Lepidocrocite-Type Layered TiO_2 Structures. *ACS Appl. Energy Mater.* **2018**, *1* (5), 2078–2086.
(49) Yuan, H.; Besselink, R.; Liao, Z.; ten Elshof, J. E. The Swelling Transition of Lepidocrocite-Type Protonated Layered Titanates into Anatase under Hydrothermal Treatment. *Sci. Rep.* **2015**, *4* (1), 4584.